Climate network stability measures of El Niño variability

Qing Yi Feng; Henk A. Dijkstra

Check for updates

CrossMark

View Online

Export Citation

Articles You May Be Interested In

Climate network stability measures of El Niño variability

Qing Yi Feng[a)] and Henk A. Dijkstra
Department of Physics and Astronomy, Institute for Marine and Atmospheric Research Utrecht (IMAU), Utrecht University, Utrecht, The Netherlands

One of the crucial aspects that is currently limiting the success of El Niño predictions is the stability of the slowly varying Pacific climate state. This property determines whether or not sea surface temperature perturbations will be amplified by coupled ocean-atmosphere feedbacks. The so-called Bjerknes stability index has been developed for this purpose, but its evaluation is severely constrained by data availability. Here, we present new network based measures of the stability of the Pacific climate state. These measures can be evaluated by using only sea surface temperature data and efficiently indicate whether positive feedbacks of perturbations to the climate state will occur. *Published by AIP Publishing.* [http://dx.doi.org/10.1063/1.4971784]

The El Niño phenomenon is a key mode of variability in the Earth System. One of the crucial aspects in predictions of El Niño variability is the stability of the Pacific climate state. Here, we develop and explore the performance of new network based measures monitoring this stability property. The great advantage of the measures is that they are easily computed using only sea surface temperature data.

I. INTRODUCTION

The El Niño-Southern Oscillation (ENSO) in the equatorial Pacific Ocean is the most pronounced mode of interannual climate variability involving coupled ocean-atmosphere processes. The observed development of the equatorial Pacific sea surface temperature (SST) during the years 2014–2015 has highlighted the challenges in predicting strong El Niño events at lead times beyond six months.

The eastern Pacific equatorial upper ocean heat content anomalies were very large during March–May 2014, and models predicted strong El Niño conditions by the end of 2014 (http://www.cpc.ncep.noaa.gov/). However, the atmospheric response to the associated SST anomalies did not involve any strong feedback. As a consequence, equatorial Pacific SST anomalies remained relatively small in December 2014. The peak of the NINO3.4 index (the area-averaged SST anomalies over the region 120°W–170°W × 5°S–5 °N) in December 2014 even did not exceed 1.0 °C. Early in 2015, warming conditions appeared near the dateline leading to weak El Niño conditions. In March 2015, the models predicted that the NINO3.4 index would not exceed 1.0 °C by the end of 2015. By mid-May, this model estimate had increased to 1.5 °C, but in reality, the NINO3.4 index even exceeded 3.0 °C at the end of November 2015 associated with one of the strongest events ever measured.[1]

After more than thirty years of active research and with a good understanding of the basic ENSO processes since the 1990s, the prediction skill (with a lead time of 6 months or more) of the models in 2014–2015 appears disappointing. Since ENSO has large effects on the regional weather in large parts of the world with severe impacts on nature and society, it is important to understand the factors influencing this prediction skill.

Much of the theory of ENSO was elucidated using the Zebiak and Cane (ZC) model,[2] which is thought to capture the basic processes of ENSO development. Many studies using this model have led to the recharge-discharge oscillator view of ENSO, where positive Bjerknes feedbacks are responsible for the amplification of SST anomalies and ocean adjustment provides a negative delayed feedback.[3,4] The strength of these feedbacks is measured by a coupling strength, here indicated by μ, which is proportional to the change in wind stress due to a change in SST.

In the ZC model, the (steady or seasonal) background Pacific climate, e.g., provided by observations, becomes unstable when the strength of the coupled processes exceeds a critical value. The critical boundary $\mu = \mu_c$ is, in dynamical systems theory language, a Hopf bifurcation (steady background state) or a Neimark-Sacker bifurcation (seasonal background state). When $\mu > \mu_c$, the oscillatory motion develops spontaneously[5,6] and the spatial pattern of the resulting variability is usually referred to as the ENSO mode. The critical boundaries μ_c have been explicitly calculated for ZC-type models[7,8] and shown to involve the same oscillatory ENSO mode for both annual mean and seasonal background states.

When conditions are such that $\mu < \mu_c$, the ENSO mode is damped and can only be excited by noise.[9,10] This noise is a representation of unresolved processes, such as westerly wind bursts in the central Pacific.[11] While these processes may actually depend on the large scale SST patterns of the Pacific[12] and hence the noise may be state dependent, many of the studies with ZC-type models have focussed on additive noise in the wind-stress field.[13] The coupled ocean-atmosphere behavior described in these studies qualitatively resembles that of a stochastic Hopf bifurcation, where the ENSO variability is dependent on the noise amplitude below criticality. Hence, although the noise driven and sustained ENSO variability views are sometimes considered to be two

different ENSO mechanisms, both are easily reconcilable:[14] it just depends on whether the background climate is stable ($\mu < \mu_c$) or unstable ($\mu > \mu_c$).

A complication arises because both the background state and the growth/decay of the ENSO mode are controlled by similar coupled processes.[8] In addition, the background climate is also affected by processes outside of the Pacific basin such as those at midlatitudes and in the equatorial Indian Ocean and Atlantic Ocean.[15] Together with slow changes in the external radiative forcing, the background state has a strong non-stationary component on decadal-to-interdecadal time scales. Hence, in more realistic Global Climate Models, such as those used in the CMIP5 project,[16] the critical boundary separating stable and unstable background states is not easy to identify.

A measure used to quantify the stability of the Pacific climate is the Bjerknes stability (BJ) index,[16–18] which is based on the recharge-discharge oscillator framework.[19] However, the calculation of the BJ index requires a comprehensive dataset of the mean ocean currents, the mean ocean upwelling, and the zonal and vertical gradients of the mean upper ocean temperature. Moreover, determining the linear correlations between variables in the BJ index formulation requires relatively long time series. Thus, the BJ index cannot be used in cases when only SST observations (such as in the period before the TAO/TRITON array) are available or when observational time series are relatively short. Because SST is the crucial quantity connecting atmosphere and ocean dynamics, this field should contain enough information to determine the stability of the Pacific climate.

Diagnosing the stability of the Pacific climate is key to improve the skill in future ENSO predictions,[20–22] and a more practical measure (than the BJ index) of the stability of the background state based on only SST data is urgently needed. In this paper, we develop new measures of the stability of the Pacific climate. We build on the success of Climate Network (CN) approaches to efficiently monitor changes in spatial correlations of the atmospheric surface temperature.[23–26] The central two elements of this approach are CN reconstruction and subsequent CN analysis.[27,28] Efficient software packages, such as *Pyunicorn*[29] and *Par@graph*,[30] are now available for this task. Network approaches have been used for studying past ENSO behavior,[31] to develop improved methods for ENSO prediction[32] and to analyse projected changes in ENSO over the next century.[33]

Our strategy is to use the ZC model as a reference model because the stability boundary μ_c (and the BJ index) can be determined precisely for this model. In Section II, the reconstruction methods of two different types of climate networks, correlation and recurrence networks, and the network measures used are described. These measures are applied in Section III to the output of the ZC model to test their performance and subsequently applied to observations. A summary and discussion of the results concludes the paper (Section IV).

II. MODEL, DATA, AND NETWORK METHODS

In this section, we briefly describe the main elements of the Zebiak-Cane model, the observational and CMIP5 model data which we analysed, and the methods of network reconstruction and analysis used.

A. The Zebiak and Cane model

This model is a representation of the coupled ocean-atmosphere flow on the equatorial β-plane in the Pacific with planetary vorticity gradient β_0. The ocean is bounded by meridional walls at the west ($x = 0$) and the east ($x = L$) coast. The ocean component of the model consists of a well-mixed surface layer of mean depth H_1 embedded in a shallow water layer of mean depth $H = H_1 + H_2$ having a constant density ρ. Only long wave motions are considered and the deep ocean (having a constant density $\rho + \Delta\rho$) is assumed to be at rest.

We here provide only the main equations and a brief description; details of the model formulation can be found in Zebiak and Cane.[2] The equations for the shallow-water layer flow are[2,34]

$$\frac{\partial u}{\partial t} + a_m u - \beta_0 y v + g' \frac{\partial h}{\partial x} = \frac{\tau^x}{\rho H}, \tag{1a}$$

$$\beta_0 y u + g' \frac{\partial h}{\partial y} = 0, \tag{1b}$$

$$\frac{\partial h}{\partial t} + a_m h + c_0^2 \left(\frac{\partial u}{\partial x} + \frac{\partial v}{\partial y} \right) = 0, \tag{1c}$$

where u and v are the horizontal velocities and h is the thickness of the layer. In these equations, τ^x is the zonal wind stress, $g' = g\Delta\rho/\rho$ is the reduced gravity, $c_0 = \sqrt{g'H}$ is the phase speed of the first oceanic baroclinic Kelvin mode, and a_m is a linear damping coefficient. The boundary conditions at the zonal boundaries are

$$\int_{-\infty}^{\infty} u(0, y, t)\, dy = 0, \quad u(L, y, t) = 0, \tag{2}$$

and all variables are bounded in the meridional (y) direction. The equations for the surface layer velocities (u_s, v_s) are

$$a_s u_s - \beta_0 y v_s = \frac{H_2}{H} \frac{\tau^x}{\rho H_1}, \tag{3a}$$

$$a_s v_s - \beta_0 y u_s = 0, \tag{3b}$$

where a_s is a linear damping coefficient.

The evolution of the sea surface temperature T is described by

$$\frac{\partial T}{\partial t} + a_T(T - T_0) + \frac{w_1}{H_1}\mathcal{H}(w_1)(T - T_s(h))$$
$$+ u_1 \frac{\partial T}{\partial x} + v_1 \frac{\partial T}{\partial y} = 0, \tag{4}$$

where a_T is a linear damping coefficient, $u_1 = u_s + u$, $v_1 = v_s + v$ and $w_1 = w_s + w$, $\mathcal{H}$ are the Heaviside functions, and T_0 is the radiation equilibrium temperature. The subsurface temperature T_s depends on the vertical temperature distribution and hence on the thermocline depth h according to

$$T_s(h) = T_{s0} + (T_0 - T_{s0})\tanh\left(\frac{h + h_0}{\hat{H}}\right), \qquad (5)$$

where h_0 and $\hat{H}$ represent control parameters for the steepness and the offset of the T_s profile, and T_{s0} is the characteristic temperature being upwelled into the surface layer.

The ocean model is coupled to a Gill atmosphere model[35] with zonal and meridional velocities (u_a, v_a), geopotential height ϕ, and a linear damping coefficient A_m. The atmosphere is driven by heat fluxes from the ocean that depend linearly on the anomalies of sea surface temperature T with respect to the radiation equilibrium temperature T_0, with proportionality constant α_T. The governing equations of the atmosphere model are

$$\frac{\partial u_a}{\partial t} + A_m u_a - \beta_0 y v_a - \frac{\partial \phi}{\partial x} = 0, \qquad (6a)$$

$$\frac{\partial v_a}{\partial t} + A_m v_a + \beta_0 y u_a - \frac{\partial \phi}{\partial y} = 0, \qquad (6b)$$

$$\frac{\partial \phi}{\partial t} + A_m \phi - c_a^2 \left(\frac{\partial u_a}{\partial x} + \frac{\partial v_a}{\partial y}\right) = \alpha_T(T - T_0), \qquad (6c)$$

where c_a is the phase speed of the atmospheric Kelvin wave.

The zonal wind stress τ^x is decomposed into an external and a coupled contribution[8]

$$\tau^x = \tau^x_{ext} + \tau^x_c. \qquad (7)$$

The coupled part of the wind stress is assumed to be proportional to the zonal wind field u_a, i.e., $\tau^x_c = \rho H \gamma_\tau u_a$, with γ_τ a constant coefficient. The external wind stress τ^x_{ext} does not depend on the coupled feedbacks within the basin and can be thought of to represent the easterly stress component due the Hadley circulation and it is assumed constant in the zonal direction.[36] In the meridional direction, the external wind stress is assumed to be symmetric with respect to the equator, having the form[8]

$$\tau^x_{ext} = -\tau_0 e^{\left[-\frac{1}{2}\left(\frac{y}{L_a}\right)^2\right]}, \qquad (8)$$

where τ_0 is a typical amplitude of the external wind stress and L_a is the atmospheric Rossby deformation radius.

In order to obtain the proper climatology of the present-day Pacific together with realistic ENSO variability, the standard parameter values as in Table I are used. The coupling parameter μ_0 is a dimensionless product of the dimensional parameters and is given by

$$\mu_0 = \mu \frac{\alpha_T \gamma_\tau \Delta T L^2}{c_o^2 c_a^2}, \qquad (9)$$

where ΔT is a typical SST difference over the basin, here taken as $\Delta T = 1\,^\circ C$. The dimensionless parameter μ is used below to control the strength of the coupling.

To solve the model equations numerically, variables are expanded into spectral basis functions, with Chebychev polynomials in the zonal direction and Hermite functions in the meridional direction.[8] The solutions are then obtained by a collocation method with the N_x collocation point in the zonal

TABLE I. Values of dimensional parameters used in the ZC model.

$L = 1.5 \times 10^7$	(m)	$c_0 = 2$	(m/s)
$c_a = 30$	(m/s)	$H = 200$	(m)
$H_1 = 50$	(m)	$H_2 = 150$	(m)
$T_0 = 0.01$	[Pa]	$T_{s0} = 23.0$	(°C)
$a_m = 1.3 \times 10^{-8}$	(s^{-1})	$T_0 = 30.0$	(°C)
$a_s = 5.0 \times 10^{-6}$	(s^{-1})	$\hat{H} = 40$	(m)
$a_T = 9.25 \times 10^{-8}$	(s^{-1})	$h_0 = 20$	(m)
$A_m = 2.5 \times 10^{-6}$	(s^{-1})	$\beta_0 = 2.2 \times 10^{-11}$	(ms)$^{-1}$
$g' = 0.02$	(ms^{-2})	$L_a = 1.5 \times 10^6$	(m)
$\alpha_T = 5.4 \times 10^{-3}$	(m^2 s^{-3} K^{-1})	$\gamma_\tau = 6.5 \times 10^{-6}$	(s^{-1})

direction and N_y in the meridional direction. All results in Section III A were computed using $N_x = 30$ and $N_y = 31$ which gives sufficiently accurate solutions.[8]

B. Observational and CMIP5 model data

For the observational data, we used the Hadley Centre Sea Ice and Sea Surface Temperature (HadISST) dataset[37] over the period December 1951–November 2015. The data were interpolated on a 31×30 grid within the domain (140 °E, 280 °E) × (20 °S, 20 °N).

The CMIP5 (5th Coupled Model Intercomparison Project) is an internationally coordinated activity to perform climate model simulations for a common set of experiments across all the world's major climate modelling centres.[38] In this paper, we use data of historical and Representative Concentration Pathway (RCP) scenario simulations, as discussed in Kim et al.,[16] from five different CMIP5 models: Coupled Physical Model version 3 (GFDL-CM3) and the Earth System Model (GFDL-ESM2M) provided by the Geophysical Fluid Dynamics Laboratory, ModelE/Russell coupled atmosphere-ocean model (GISS-E2-R) by the NASA Goddard Institute for Space Studies, Norwegian Earth System Model (NorESM1-ME) by the Norwegian Climate Centre, and the Community Earth System Model version 4 (CCSM4) by the National Center for Atmospheric Research.

C. Climate network reconstruction and analysis

Climate scientists have been long interested in studying the statistical correlation between climatological variables for gaining a good understanding of the large-scale dynamics of the climate system.[39] By investigating the correlation structures of global or regional fields of observables, such as surface air temperature, pressure, or geopotential height, a better view on spatial as well as temporal patterns accounting for a large fraction of the fields' variance could be given. A correlation Climate Network (CN) based on statistical correlation offers a complementary analysis by applying the measures and techniques of complex network theory to the study of climate dynamics.[40,41] There are generally three steps of this methodology: first, create a network from gridded climate data; then, build links from correlations of the time series; next, investigate the dynamics of the climate system through the properties of the network.

There are many measures for quantifying the correlations between two time series. For example, in a Pearson

Correlation Climate Network (PCCN), the Pearson correlation is used to quantify the correlations of time series, whereas in a Mutual Information Climate Network (MICN), the mutual information is used;[42] in this paper, we only use PCCNs. Suppose that the observables like SST, either from observations or model simulations, are gathered at N grid points. In this way, the data can be described by an $n \times N$ matrix F, in which each column vector $\mathbf{p}_i = (p_i(t_1), \ldots, p_i(t_n))^T$ at a grid point ($i = 1, \ldots, N$) contains a time series of length n. To reconstruct a PCCN, the linear Pearson correlation coefficient is used to determine the correlation between the time series of observables at two grid points i and j. The elements R_{ij}^C of the correlation matrix R^C are given by

$$R_{ij}^C = \frac{\sum\limits_{k=1}^{n} p_i(t_k)p_j(t_k)}{\sqrt{\left(\sum\limits_{k=1}^{n} p_i^2(t_k)\right)\left(\sum\limits_{k=1}^{n} p_j^2(t_k)\right)}}. \quad (10)$$

Each grid point is seen as a node in a network, and the link between a pair of nodes (i, j) is determined by R_{ij}^C. In a PCCN, two nodes i and j have an unweighted link if the absolute value of their correlation coefficient R_{ij}^C is above a certain threshold value ϵ_C, which gives a statistical significance above the 95% level. All links are then represented in the $N \times N$ adjacency matrix A^C, which can be determined from the correlation matrix R^C using

$$A_{ij}^C = \mathcal{H}(|R_{ij}^C| - \epsilon_C) - \delta_{ij}, \quad (11)$$

where δ_{ij} is the Kronecker delta introduced to avoid self-loops in the network and $\mathcal{H}$ is the Heaviside function.

By reconstructing a PCCN, the (linear) correlation structure of climate observables is mapped into a graph. The underlying dynamics of the climate system can be analysed through network properties (see e.g., Table 4.2 in Donges (2013)[41]). For example, a measure of the connectivity of a node i in a graph with adjacency matrix A is given by the degree d_i, with

$$d_i = \sum_{j=1}^{N} A_{ij}. \quad (12)$$

When a node has a high degree it means that it is connected to a larger amount of other nodes in the network; a low degree node is "isolated" in the network.

Recurrence is a fundamental property of a dynamical system's phase space, and recurrence properties can be easily visualized by the so-called recurrence plots obtained from a single scalar property of a trajectory of a dynamical system.[43,44] The recurrence plot based techniques are very useful for the analysis of short and non-stationary data[45] and have been used to detect climate transitions.[46]

Suppose the time series of an observable, for example, the NINO3.4 index, is represented by $x(t)$. One then uses an m-dimensional time delay embedding of $x(t)$ with delay τ to generate the $m-$ dimensional trajectory[47] $\mathbf{x}^{(m)}(t_k) = (x(t_k), x(t_k + \tau), \ldots, x(t_k + (m-1)\tau))$, $k = 1, \ldots, N$. The binary recurrence matrix R^R is then defined through

$$R_{ij}^R = \mathcal{H}(\epsilon_R - ||\mathbf{x}(t_i) - \mathbf{x}(t_j)||), \quad (13)$$

where $\mathcal{H}$ is the Heaviside function, $|| \cdot ||$ denotes a suitable norm in the embedded phase space, and ϵ_R is a recurrence threshold. Like the adjacency matrix (Eq. (11)) which is the basis of complex network analysis, the binary recurrence matrix (Eq. (13)) is also square, binary, and symmetric. This striking similarity has led to the definition of a recurrence network[45,47] which has an adjacency matrix

$$A_{ij}^R = R_{ij}^R - \delta_{ij}. \quad (14)$$

In the context of climate studies, such networks are referred to as Recurrence Climate Networks (RCNs).

The nodes in an RCN represent state vectors, and the links indicate the proximity relationship between them. Due to the natural interpretation of nodes and links, many topological characteristics of an RCN closely capture the fundamental phase space properties of the climate system.[47] A measure for the density of recurrence points in an RCN is the recurrence rate (ρ_R) given by

$$\rho_R = \frac{1}{N^2} \sum_{i,j=1}^{N} A_{ij}^R. \quad (15)$$

Many network properties of recurrence networks (skewness, kurtosis, etc.) have been used to analyse time series.[48] Here, we use a measure for the continuity of phase space density in an RCN, i.e., the assortativity α_R, showing the preference for the nodes to attach to others that are similar in degree. The assortativity can be quantified by the Pearson correlation coefficient of the degree between pairs of linked nodes,[49] i.e.,

$$\alpha_R = \frac{\dfrac{1}{l}\sum\limits_{j>i} d_i d_j A_{i,j} - \left[\dfrac{1}{l}\sum\limits_{j>i}\dfrac{1}{2}(d_i + d_j)A_{i,j}||\right]^2}{\dfrac{1}{l}\sum\limits_{j>i}\dfrac{1}{2}\left(d_i^2 + d_j^2\right)A_{i,j} - \left[\dfrac{1}{l}\sum\limits_{j>i}\dfrac{1}{2}(d_i + d_j)A_{i,j}\right]^2}, \quad (16)$$

where l is the total number of links in the RCN. It turns out (see Section III) that the different ENSO behavior can be most efficiently distinguished in the two-dimensional plane spanned by the assortativity (rather than using the skewness) and the recurrence rate.

III. RESULTS

We will first consider the network measures for the Zebiak-Cane model (Section III A) and then apply them to observations and CMIP5 data (Section III B).

A. The ZC model

In the deterministic ZC model, with the parameters as in Table I, a Hopf bifurcation occurs at $\mu = \mu_c = 3.0$. When the coupling strength is smaller than μ_c, for example, $\mu = 2.7$, the system is in the subcritical regime where it exhibits a damped ENSO oscillation when no noise is

present. This is shown in the behavior of the NINO3.4 index (red curve) in Fig. 1(a). When the coupling strength is increased to just above the critical value ($\mu = 3.02 > \mu_c$), the system will enter the supercritical regime where the NINO3.4 index displays an interannual oscillation (red curve in Fig. 1(c)) and the spectrum shows a peak at about 4 years (red curve in Fig. 1(d)).

Next, an additive red noise product is used for the zonal wind-stress forcing.[13] The extended reconstructed sea surface temperature (ERSST) over the Pacific Ocean for the period of 1978–2004[50] and the Florida State University pseudo-wind-stress data for the same period[51] are used to calculate the residual of the wind stress. The zonal wind stress anomalies that are linearly related to NINO3.4 anomalies are subtracted from the zonal wind-stress anomalies. The resulting residual is decomposed into its empirical orthogonal functions (EOFs), and the first and second EOFs and their principal components (PCs) are shown in Fig. 2. The first EOF (Fig. 2(a)) represents the residual zonal wind response in the eastern Pacific. The second EOF (Fig. 2(b)) captures the pattern of westerly wind bursts which are generally

located west of the date line.[11] For example, the second PC (PC2) shows (Fig. 2(d)) a strong westerly wind event in March 1997, in agreement with other analyses.[11,52]

The stochastic component of the zonal wind-stress forcing τ_n^x can then be written as

$$\tau_n^x(x, y) = a_1 E_1(x, y) + a_2 E_2(x, y), \qquad (17)$$

where the $E_i, i = 1, 2$ are the patterns of the first and second EOF and the a_i are determined from the fit of an autoregressive model (AR1) $x_{i,t}$ to the PC$_i$ time series using

$$x_{i,t+1} = a_i x_{i,t} + \sigma_i \epsilon_{i,t}. \qquad (18)$$

Here, each a_i is the lag-1 autocorrelation of PC$_i$, and the term $\sigma_i \epsilon_{i,t}$ represents white noise with a variance σ_i. This stochastic component is added to the deterministic zonal wind stress (Eq. (8)), and the response of the ZC model is shown as the black curves in Figs. 1(a) and 1(b) (subcritical) and 1(c) and 1(d) (supercritical). In the subcritical regime, the red noise forcing is necessary to excite the ENSO variability, while in the supercritical regime, the red noise forcing simply causes
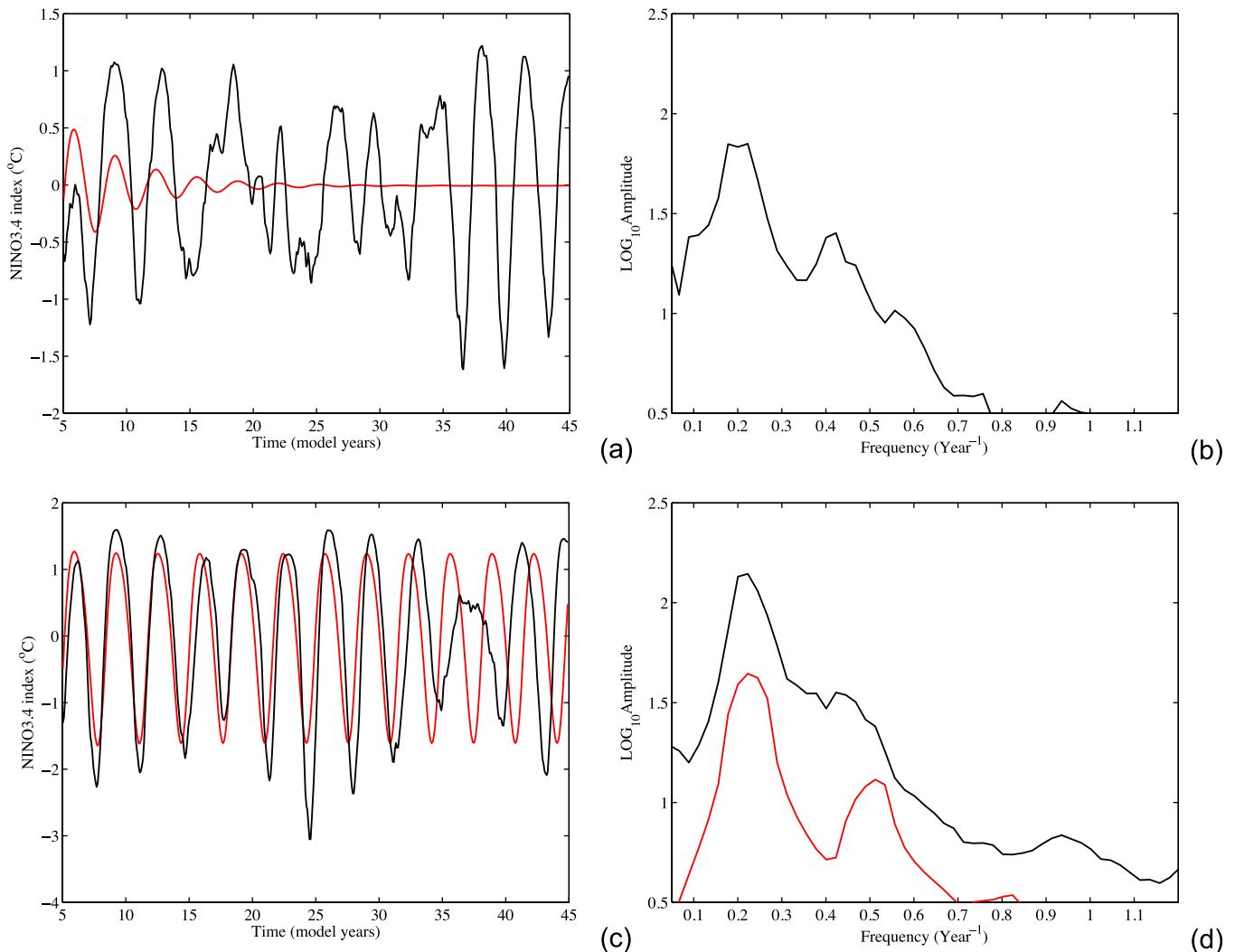

FIG. 1. The response of the Zebiak and Cane (ZC) model. Red curves are for the deterministic model, and black curves are for the stochastic model with red noise wind-stress forcing. (a) The NINO3.4 index at a coupling strength $\mu = 2.7$, and (b) the amplitude spectrum for (a), (c) same as (a) but at $\mu = 3.02$, and (d) the amplitude spectrum for (c).
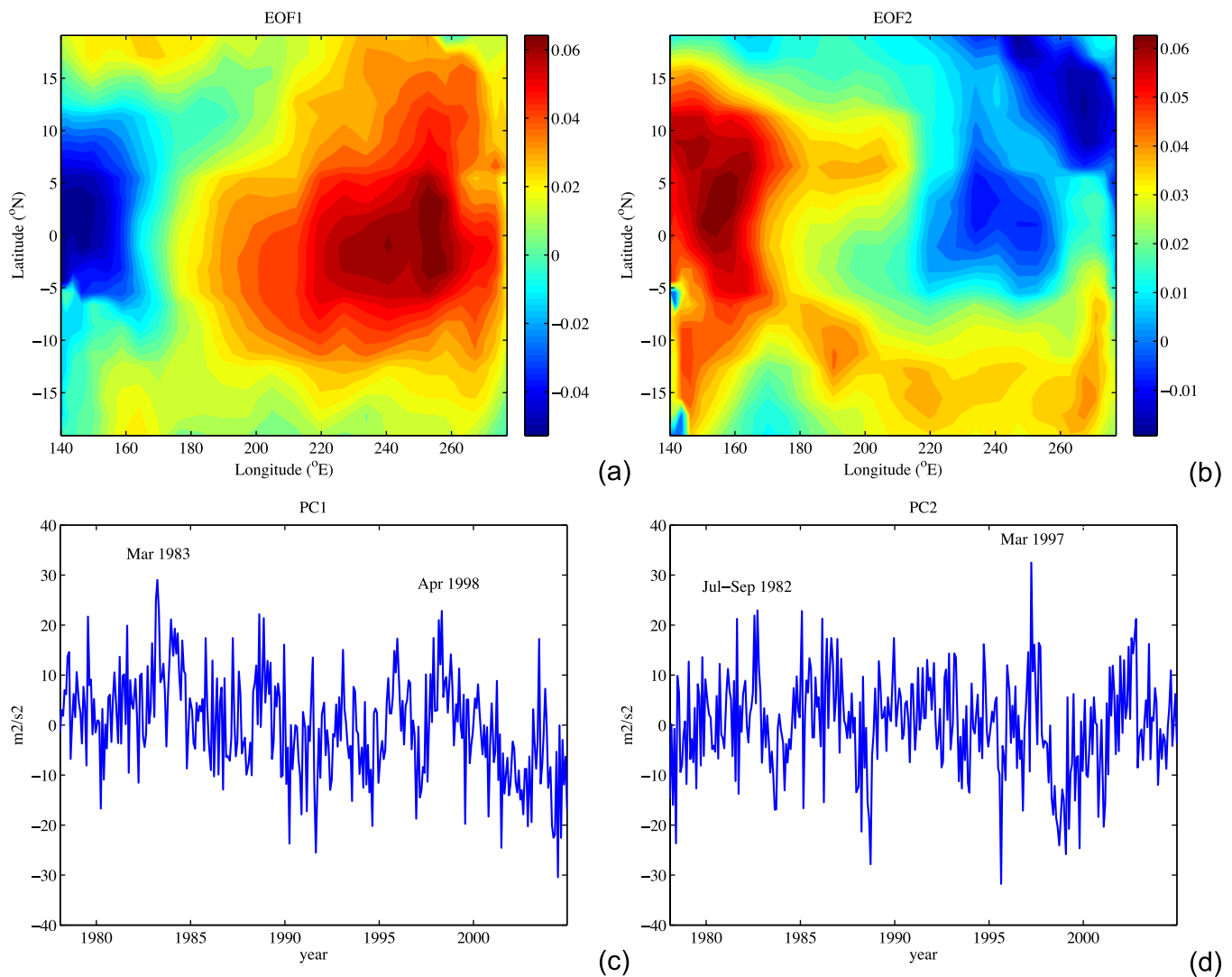
FIG. 2. (a) The first empirical orthogonal function (EOF) of the zonal wind-stress residual, accounting 11.9% of the variance. (b) The same as (a) but the second EOF, accounting for 11.6% of the variance. (c) The first principal component (PC1) of the wind stress residual. (d) The same as (c) but the second principal component (PC2).

a higher amplitude of ENSO variability; these results are similar to those provided by Roulston and Neelin.[13]

Next, the ZC-model output of 11 simulations, 540 months (45 years) each, at different values of the coupling strength μ (2.70, 2.80, 2.90, 2.95, 2.98, 3.00, 3.02, 3.10, 3.15, 3.25, and 3.40) was generated. The PCCNs reconstructed for each value of μ have 30 (longitude) × 31 (latitude)= 930 nodes within the domain (140 °E, 280 °E) × (20 °S, 20 °N). Here, the threshold value $\epsilon_C = 0.5$ was used which guarantees that the links in the PCCN are based on significant ($p < 0.05$) correlations. The degree fields of the PCCNs reconstructed for four values of μ are shown in Figs. 3(a)–3(d). When the coupling strength μ is increased from the subcritical $\mu < \mu_c$ to the supercritical regime $\mu > \mu_c$, more nodes in the region between 220 °E and 280 °E get a higher degree. When the critical boundary μ_c is approached, the spatial pattern of the anomalies is perhaps more reminiscent of the ENSO mode, leading to large-scale coherence which is efficiently captured by the network degree field. Another distinct change of the degree fields (Figs. 3(a)–3(d)) is that the patterns of equatorially symmetric Rossby waves

are becoming more prominent when the background state enters the supercritical regime.

Histograms of the degree fields (the degree distributions) for two different values of μ are plotted in Figs. 4(a) and 4(b). For $\mu = 2.7 < \mu_c$ (Fig. 4(a)), the degree distribution is bimodal, where the first peak represents the low degree nodes in Fig. 3(a) and the second peak (located near a degree of 250) represents the high degree nodes. When μ is increased (Fig. 4(b)), a peak at a degree of 400 occurs representing the higher degree nodes in Fig. 3(c), because the ENSO mode becomes more dominant in the SST anomalies when the background climate moves into the supercritical regime.[53,54]

The changes in the degree distributions with μ can be effectively measured by the skewness of the degree distribution S_d. When the mass of the distribution is concentrated more to the right like in Fig. 4(b), this results in a lower skewness value. Hence, S_d is monotonically decreasing with increasing μ, as shown as the blue curve in Fig. 4(c). There is also a good correlation between S_d and the variance of the NINO3.4 index ($Var_{NINO3.4}$, green curve) as shown in Fig.
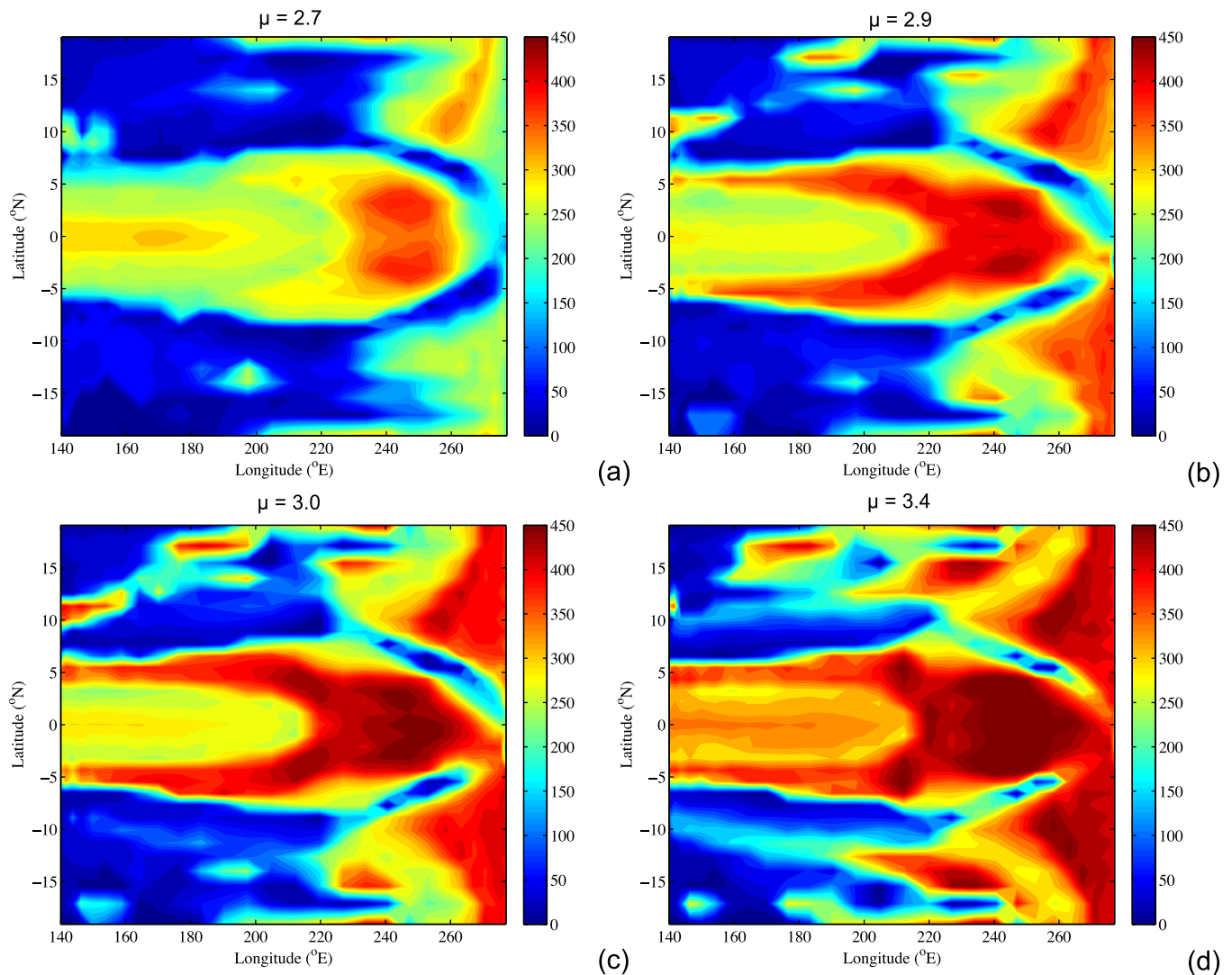
FIG. 3. (a) Degree field of the PCCN using a threshold $\epsilon_C = 0.5$ reconstructed from the ZC model data at a coupling strength $\mu = 2.7$. (b) Same as (a) but at $\mu = 2.9$. (c) Same as (a) but at $\mu = 3.0$. (d) Same as (a) but for $\mu = 3.4$.

4(c). Note, however, that at high values of S_d (stable climate, $\mu < \mu_c$), the amplitude of NINO3.4 depends on the noise.

For these ZC-model results, the BJ index was also computed in a way as described in supplementary material. The BJ index (the black curve in Fig. 4(d)) is monotonously increasing with increasing μ and crosses the zero line at about $\mu = 3.1$ which is close to μ_c. This indicates that the BJ index reasonably (but not perfectly) monitors the stability of the background state.[19] The values of different terms in the BJ index (also shown in Fig. 4(d)) indicate that the thermocline feedback is dominant (cf. supplementary material) in destabilizing the background state. It has been shown in models[16,18] and reanalysis data[16] that this feedback has been dominant during past ENSO events. Therefore, when the background Pacific climate is such that it is close to the critical boundary, long-range correlations between SST time series occur (Fig. 3(c)). These correlations are caused by the amplification of SST anomalies, mainly by the thermocline feedback, and can be measured by the PCCN degree field based index S_d (Fig. 4(c)).

We next turn to the RCNs using the NINO3.4 index at each value of μ for the same ZC-model output. We choose a time interval of 10 years of the monthly NINO3.4 index as a window to reconstruct the RCNs. All results below are for an embedding dimension $m = 2$, an embedding delay $\tau = 1$ (month), and a recurrence threshold $\epsilon_R = 0.5$. The results are robust when using values of $m = 2, 3, \tau = 1, 2$, and ϵ_R in the range $0.4 - 0.6$. By implementing a sliding-window strategy with a shift of one month, we calculated the value ranges of the recurrence rate and assortativity at different μ values, indicated by the mean values and error bars, as shown in Figs. 5(a) and 5(b). When the coupling strength μ is increasing, the recurrence rate decreases (Fig. 5(a)) and the assortativity increases (Fig. 5(b)).

Both topological characteristics of the RCNs are plotted in the space spanned by the recurrence rate and the assortativity in Fig. 5(c) for different values of μ. The subcritical regime (blue circles, $\mu = 2.7 < \mu_c$) and the supercritical regime (black dots, $\mu = 3.4 > \mu_c$) can be clearly distinguished in Fig. 5(c). The separation of the regimes is even more clear by marking the value ranges in the recurrence rate
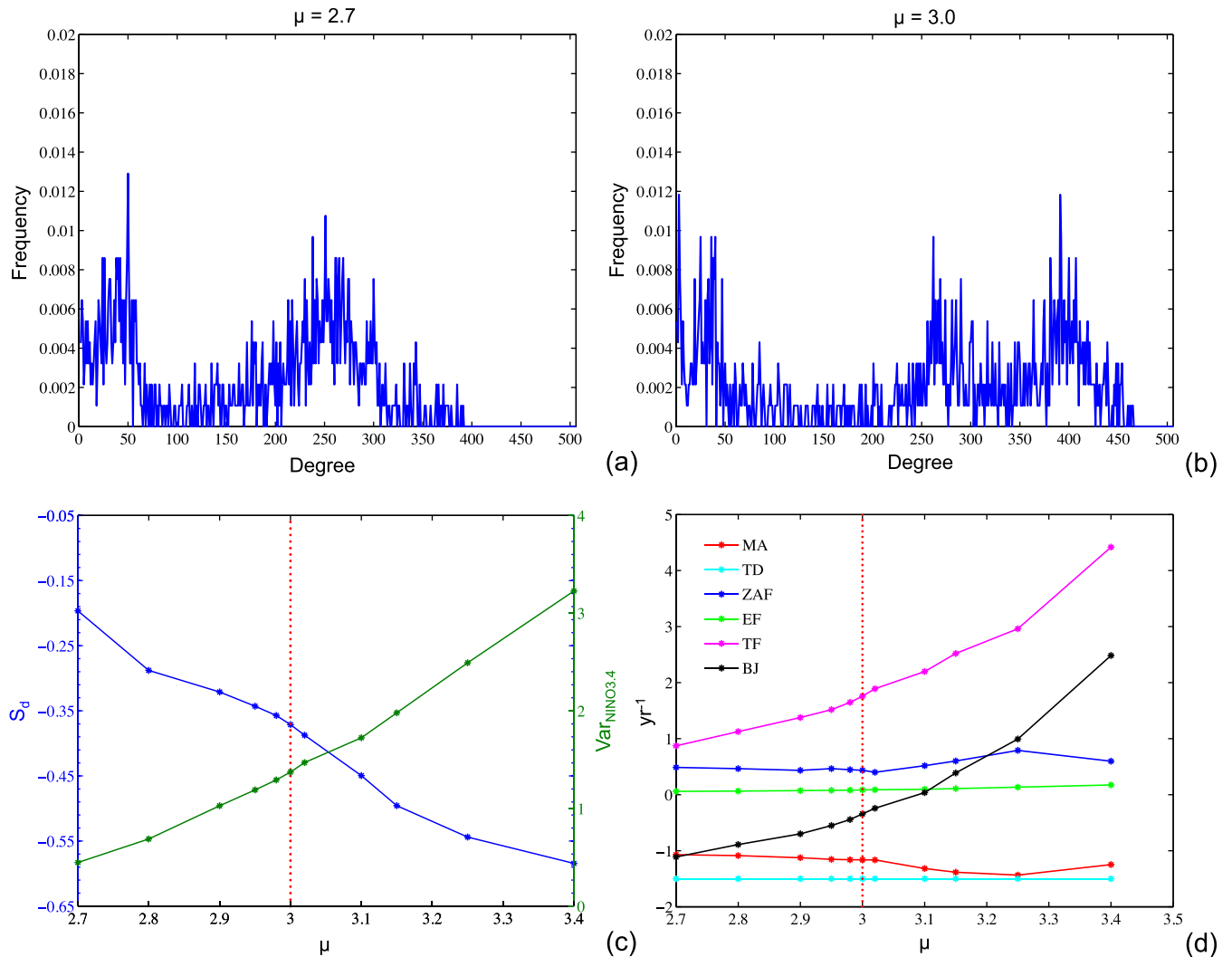
FIG. 4. (a) Degree distribution of the PCCN using a threshold $\epsilon_C = 0.5$ reconstructed from the ZC model data at the coupling strength $\mu = 2.7$. (b) Same as (a) but at $\mu = 3.0$. (c) The degree skewness index S_d (blue) and the variance of NINO3.4 index $Var_{NINO3.4}$ (green) from the ZC model as a function of μ; the red dashed line indicates the stability boundary $\mu_c = 3.0$. (d) The values of Bjerknes stability (BJ) index (cf. supplementary material) and its components from the ZC model at different μ: mean advection and upwelling (MA, red), thermal damping (TD, cyan), zonal advection feedback (ZAF, dark blue), Ekman pumping feedback (EF, green), thermocline feedback (TF, magenta), and total BJ index (BJ, black).

and the assortativity space (Fig. 5(d)). In the subcritical regime, the RCNs have a high recurrence rate and low assortativity, taking up the right lower part of the space. The supercritical regime is characterized by a low recurrence rate and a high assortativity.

B. CMIP5 model output and observations

From the PCCN analysis of the ZC model results, we have proposed a network measure S_d which monitors the stability of the Pacific background state. In addition, we have shown from the same model results that, in particular, the recurrence rate ρ_R of an RCN can distinguish subcritical from supercritical regimes. In this section, we will first use the CMIP5 model data (for which the BJ index can be computed) to demonstrate that S_d is correlated well to the BJ index. Next, we will investigate whether the information from S_d and ρ_R provides the consistent information in SST

observations and whether we can clearly distinguish noise driven from self-sustained El Niño events.

In Kim *et al.*,[16] the BJ index is computed from the CMIP5 model ensemble for the RCP8.5 greenhouse warming scenario. We reconstructed PCCNs from an ensemble of five CMIP5 GCMs (CCSM4, GFDL-CM3, GFDL-ESM2M, GISS-E2-R, and NorESM1-M) from the BEST9[16] models (in terms of their performance of historical ENSO behavior) under historical forcing (1910–2005) and the RCP8.5 scenario (2006–2100). We first removed the trends from the data with a 10-year sliding window and then used the same size of a sliding window of 50 years as used in Kim *et al.*[16] for the BJ index to calculate S_d values. The results are shown in Fig. 6 and robust to changes in the parameters used in the network reconstruction (i.e., the threshold ϵ_C). The Pearson correlations (cor) between S_d indices (blue curves) and the BJ indices (green curves) are significant ($p < 0.05$) with *cor* $= -0.857$ in CCSM4, *cor* $= -0.148$ in GFDL-CM3, *cor* $= -0.486$ in GFDL-ESM2M, *cor* $= -0.879$ in GISS-E2-R,
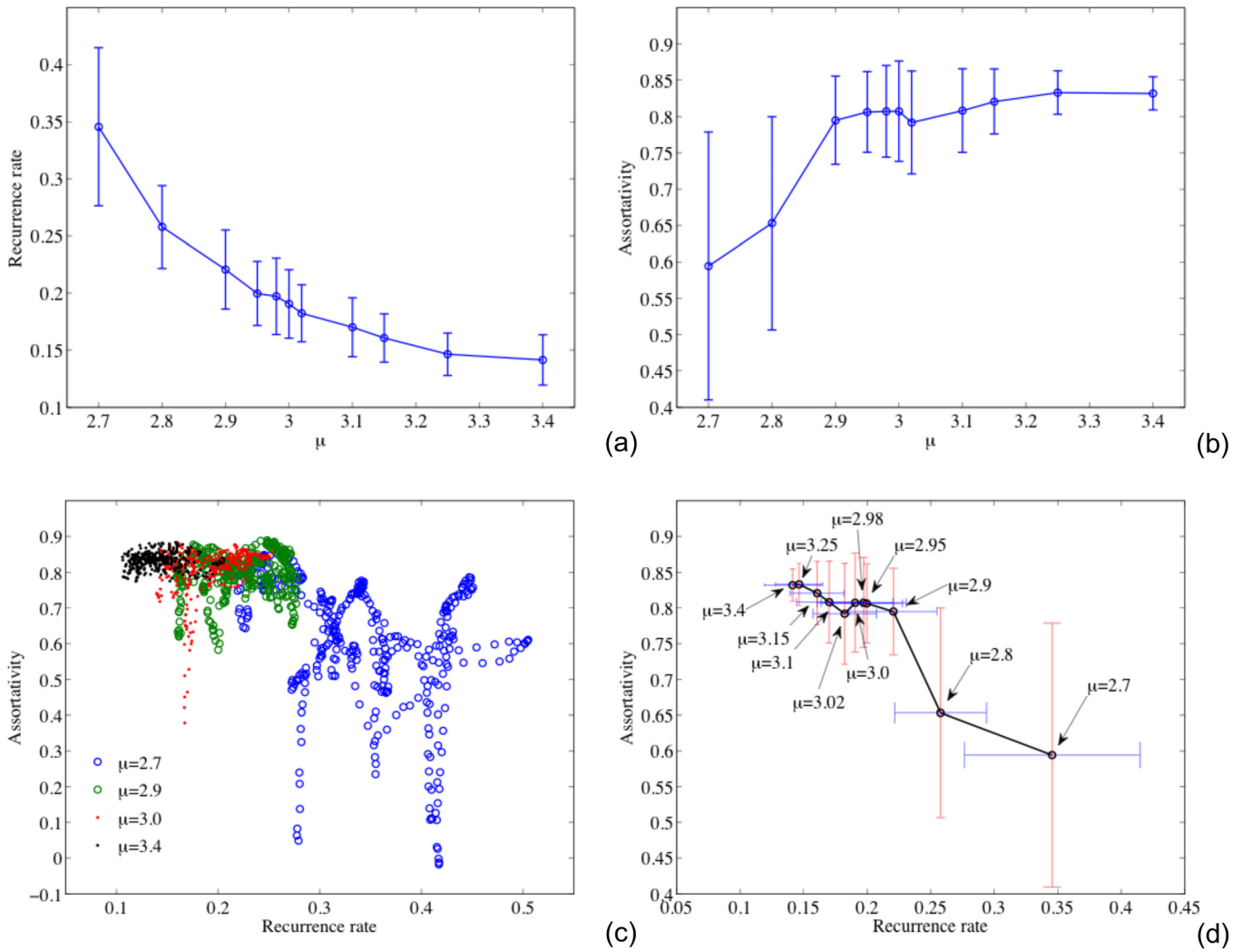
FIG. 5. (a) The mean values (with error bars indicating the range) of the recurrence rate of the RCNs reconstructed from 10-year windows of ZC model output at different coupling strengths μ. (b) Same as (a) but for the assortativity. (c) The scatter plot of the recurrence rate versus assortativity of the RCNs at the coupling strength $\mu = 2.7$ (blue circles), $\mu = 2.9$ (green circles), $\mu = 3.0$ (red dots), and $\mu = 3.4$ (black dots). (d) The mean values (with error bars indicating the range) of the recurrence rate and assortativity of the RCNs for different coupling strengths μ.

$cor = -0.689$ in NorESM1-M, and $cor = -0.868$ in the ensemble mean. The ensemble mean result in Fig. 6(f) clearly shows the anti-correlation between the S_d index and the BJ index. From 1910 to around 1960, S_d slightly increases and at the same time the BJ index decreases, which means that the stability of Pacific climate increases. From 1980 to around 2020, the S_d index drops to the lowest level, while the BJ index reaches its maximum, both indicating that the Pacific climate becomes quite unstable. From around 2040 to 2100, the S_d index increases and BJ index decreases, which indicates that the Pacific climate becomes more stable, in accordance with results in Kim et al.[16]

We also calculated the Fisher weighted mean correlation coefficient of the S_d and BJ indices in these five CMIP5 CGCMs. First, the cor values are transformed to z values using the transformation[55]

$$z = \frac{1}{2} ln \left[\frac{(1 + cor)}{1 - cor} \right].$$ (19)

Next, the Fisher weighted mean correlation coefficient $\bar{r}^{[56]}$ is computed by

$$\bar{r} = \frac{e^{\bar{z}} - e^{-\bar{z}}}{e^{\bar{z}} + e^{-\bar{z}}},$$ (20)

where $\bar{z}$ is the mean value of z in these five CMIP5 GCMs. The final result is $\bar{r} = -0.684$ which shows that the S_d index is significantly anti-correlated with the BJ index. The reason for this good anti-correlation is that a high value of S_d indicates stability of the Pacific climate state which is also measured by a low value of the BJ index (and vice versa).

Next, we calculated the network measures from observations of SST from the HadISST dataset over the period December 1951–November 2015. As the background state varies on decadal time scales, one has to resort to a sliding-window strategy. A window of 5 years is certainly too short as a full ENSO cycle is 4 years on average. However, a window of 20 years appears too long as the background from which El Niño's develop may be different from such an averaged state. Hence, we reconstructed a PCCN for every 10 years of monthly SST data and computed the value of S_d for this network. Different window lengths in the range of 8–15 years were taken, and the results are robust for these window sizes.
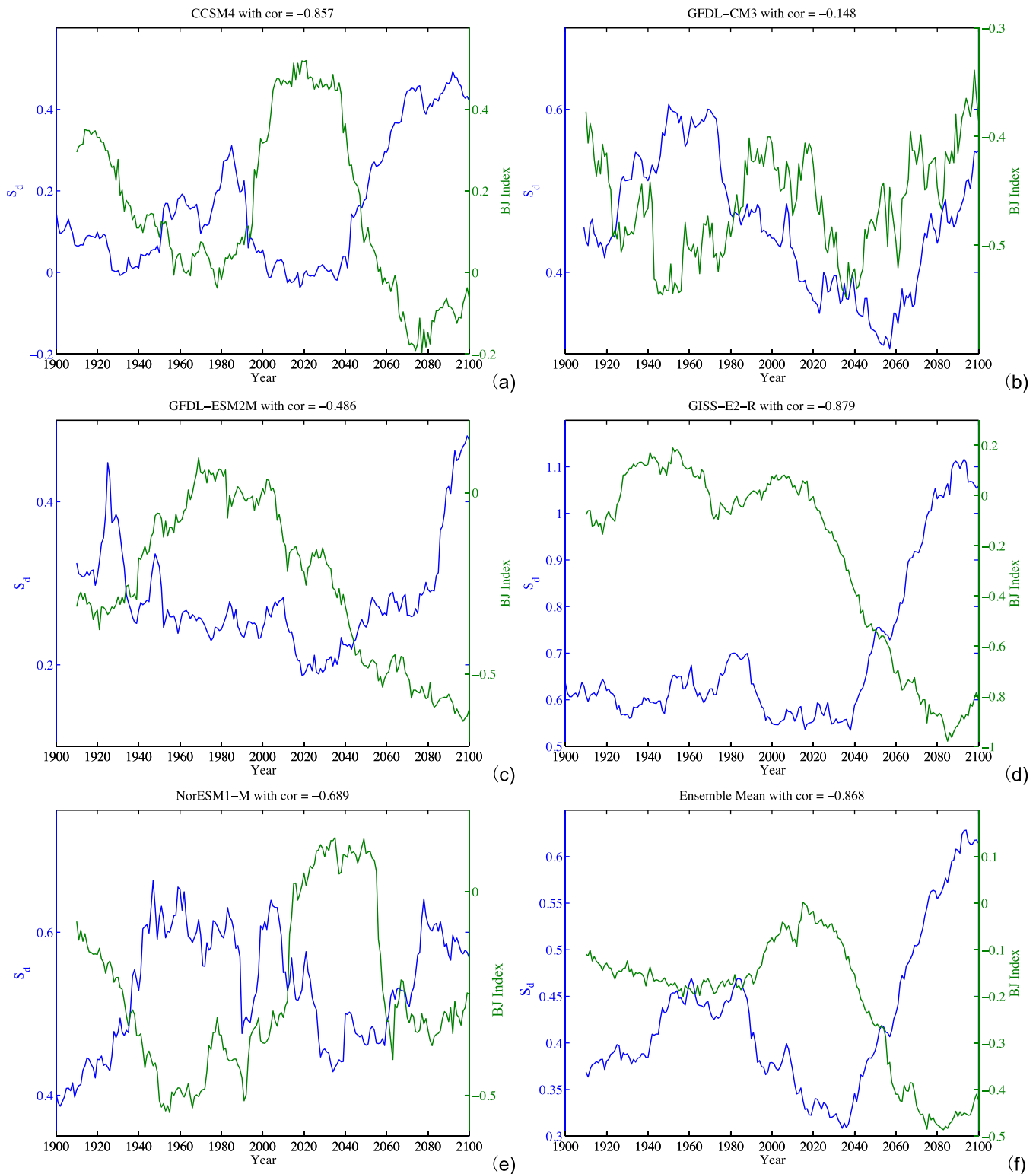
FIG. 6. The 50-year sliding window degree skewness index S_d (blue) and the BJ index (green) in Kim *et al.*[16] from the historical runs over the period 1910–2005 and the RCP8.5 simulations over the period 2006–2100 of the CMIP5 GCMs (a) CCSM4, (b) GFDL-CM3, (c) GFDL-ESM2M, (d) GISS-E2-R, (e) NorESM1-M, and (f) ensemble mean. The Pearson correlations (cor) between S_d and the BJ index stated in the subtitle are all significant ($p < 0.05$).

By implementing the sliding-window strategy with a shift of one month, we obtained a time series of S_d (black curve in Fig. 7(c)), showing the variation of the stability of the Pacific background climate over the last 60 years. The 3-month running mean of the NINO3.4 index of the same period is plotted as the green curve in Fig. 7. We also marked

the S_d values at the onset (January–March) of the 1968, 1982, 1992, 1997, and 2015 El Niño events in Fig. 7. In 1968, the January–March averaged S_d value is $S_d = 0.28$, the one in 1982 is $S_d = 0.03$, the one in 1992 is $S_d = -0.18$, the one in 1997 is $S_d = -0.35$, and the one in 2015 is $S_d = -0.03$. The relatively high value of S_d in early 1968
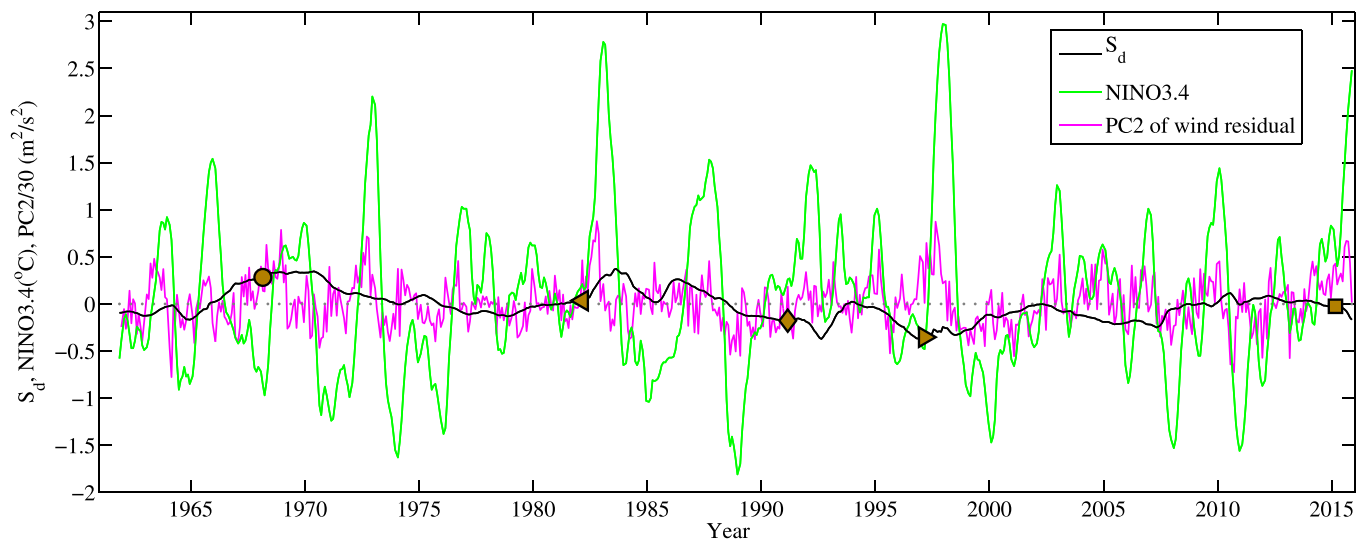
FIG. 7. The 10-year sliding window degree skewness index S_d (black curve), the 3-month running mean NINO3.4 index (green curve) from the observed SST of Dec. 1951 to Nov. 2015, and the second principal component (PC2) of the wind-stress residual (magenta curve) from the NCEP zonal windstress data of the same period. The x-axis indicates the end time of the sliding window. The brown disk indicates the mean S_d value of the window ending at January–March 1968, the brown left triangle indicates that of January–March 1982, the brown diamond indicates that of January–March 1991, the brown right triangle indicates that of January–March 1997, and the brown square indicates that of January–March 2015.

indicates that the Pacific background climate in 1968 was quite stable, and the noise must have had a large influence on the development of the 1968 El Niño event. To verify this statement, the PC2 of the wind stress residual from National Centers for Environmental Prediction (NCEP) wind stress data[57] is also plotted as the magenta curve in Fig. 7, which can be considered as representing the westerly wind bursts;[11,52] see Section III A and Fig. 2. One can see that high-noise variability occurred during early 1968. On the contrary, the 1992 El Niño event would be considered as a sustained case, because of the relatively low value of S_d and low noise variability in early 1992. Actually, the value of S_d was overall low (less stable Pacific background state) during the early 1990s with a global minimum just before 1997.

Subsequently, we studied the 1968 and 1992 events from the RCN point of view using the HadISST dataset over the same period of December 1951–November 2015. To be consistent with previous results, we reconstructed RCNs using the same 10-year windows and the same monthly sliding-window strategy as for the PCCNs, and then calculated the recurrence rate and assortativity for each RCN. The averaged recurrence plots of the RCNs over the 1968 El Niño (Fig. 8(a)) and the 1992 El Niño (Fig. 8(b)) clearly show the differences between these two events with much higher recurrence rates for the 1968 event. The "trajectories" of the events in the (ρ_R, α_R) plane show a very different behavior (Figs. 8(c) and 8(d)). Over the period 1967–1969 (Fig. 8(c)), this trajectory mainly stays in the high recurrence rate–low assortativity range. Based on the ZC model results, this would indicate a development in the subcritical regime. For 1992 (Fig. 8(d)), the trajectory stays in a low recurrence rate–high assortativity range indicating a development in the supercritical regime. The results in Figs. 8(c) and 8(d) are consistent with the information provided by the S_d index. The El Niño event in 1968 was a typical noise driven ENSO with a relatively stable Pacific background climate, while the

El Niño event in 1992 was a typical sustained case because of the unstable Pacific background climate.

Regarding the stability of the background state, the 1968 and 1992 events are the easiest to distinguish. However, it is, of course, interesting to also determine the trajectories in the (ρ_R, α_R) plane of the large amplitude El Niño events in the last few decades. In Fig. 9, these trajectories are plotted for the 1982, 1997, and 2015 events. Although the paths are quite different from each other, they all started at a low recurrence rate–high assortativity range and hence this indicates unstable background conditions. The background state of the El Niño event in 1982 (Fig. 9(a)) eventually moved to the subcritical regime, while the one in 1997 gradually moved towards the supercritical regime. This may explain why the 1997 event was followed by a relatively strong La Niña and the 1982 event was not.

IV. SUMMARY AND DISCUSSION

The Zebiak-Cane model is an intermediate complexity climate model that adequately simulates many aspects of El Niño/Southern Oscillation (ENSO) development.[2] Clearly, in this model, ENSO variability arises through an instability of the background climate state (a Hopf bifurcation) through coupled feedbacks.[58] In reality, this background state is, apart from seasonally varying, non-stationary due to long-term changes on decadal time scales[5] and it is difficult to determine its stability properties. The BJ index was designed for this task, but it cannot be computed from sole SST observations and it needs data over a long time window (see supplementary material).

In this paper, we have proposed new measures to monitor the stability of the background equatorial Pacific climate state using Pearson Correlation Climate Networks (PCCNs)[27,59] and Recurrence Climate Networks (RCNs)[44] of only sea surface temperature (SST) data. The index S_d
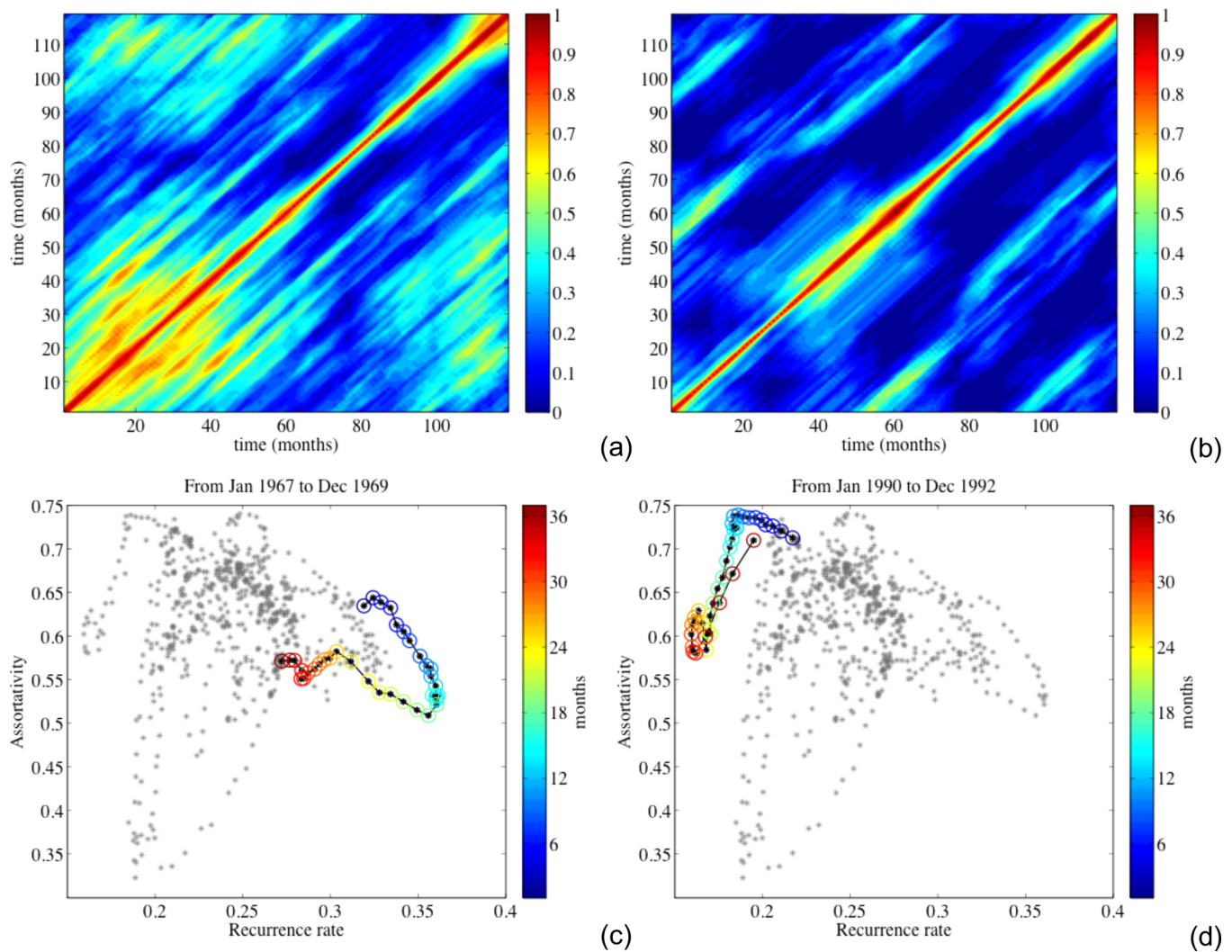
FIG. 8. (a) The averaged recurrence plot of the Recurrence Climate Networks over the time period January 1967 to December 1969. (b) Same as (a) but from January 1990 to December 1992. (c) The scatter plot of recurrence rate versus assortativity of the recurrence networks, and the colored circles highlight the development of the El Niño event in 1968, starting from January 1967 to December 1969. (d) Same as (a) but showing the development of the El Niño event in 1992, starting from January 1990 to December 1992. The recurrence networks are reconstructed from a 10-year sliding window of the HadISST data.

measures the skewness of the degree distribution of a PCCN reconstructed from significant correlations between the SST anomalies in the equatorial Pacific. The recurrence rate ρ_R measures the density of recurrence points in an RCN reconstructed from the NINO3.4 index.

We used the S_d index derived from the stochastic ZC model wherein a Hopf bifurcation has been found.[13] The index S_d is anti-correlated with the variance of the NINO3.4 index (under a fixed wind-stress noise amplitude), so a high (low) value of S_d indicates a high (low) stability of the background state. Additional support that S_d monitors the stability of the background state comes from the anti-correlated behavior (cf. Fig. 6) with the BJ index as determined for an ensemble of five CMIP5 CGCMs for the RCP8.5 scenario from the BEST9 models used in Kim *et al.*[16] Hence, our measure is consistent with the BJ index from these models and provides the same information on the possible intensification/weakening of future ENSO events.

Another network measure to analyse the stability properties of the background state was obtained from the reconstruction of recurrence networks. For the ZC model results

(cf. Fig. 5), it is found that subcritical (supercritical) regimes are characterized by the high (low) recurrence rate ρ_R and low (high) assortativity α_R. Therefore, the recurrence rate and assortativity of a recurrence plot based CN can provide additional information on the stability of the background state. Fortunately, the information of this measure is consistent with that of S_d for the SST record since 1950. Based on these measures, there appear to be typical events which are purely noise driven (such as in 1968) or purely sustained (such as in 1992).

A great advantage of the network based measures is that these are far more easy to compute than the BJ index[19] and hence they are more widely applicable. Moreover, since these measures do not require defining the thermocline or mixed layer depth, they can serve as an easier model inter-comparison tool than the BJ index. However, the disadvantage of the network measures is that it is impossible to precisely determine the boundary between subcritical and supercritical regimes. For example, one can only determine that a background state with a smaller value of S_d is more unstable than one with larger S_d, not at which value of S_d,
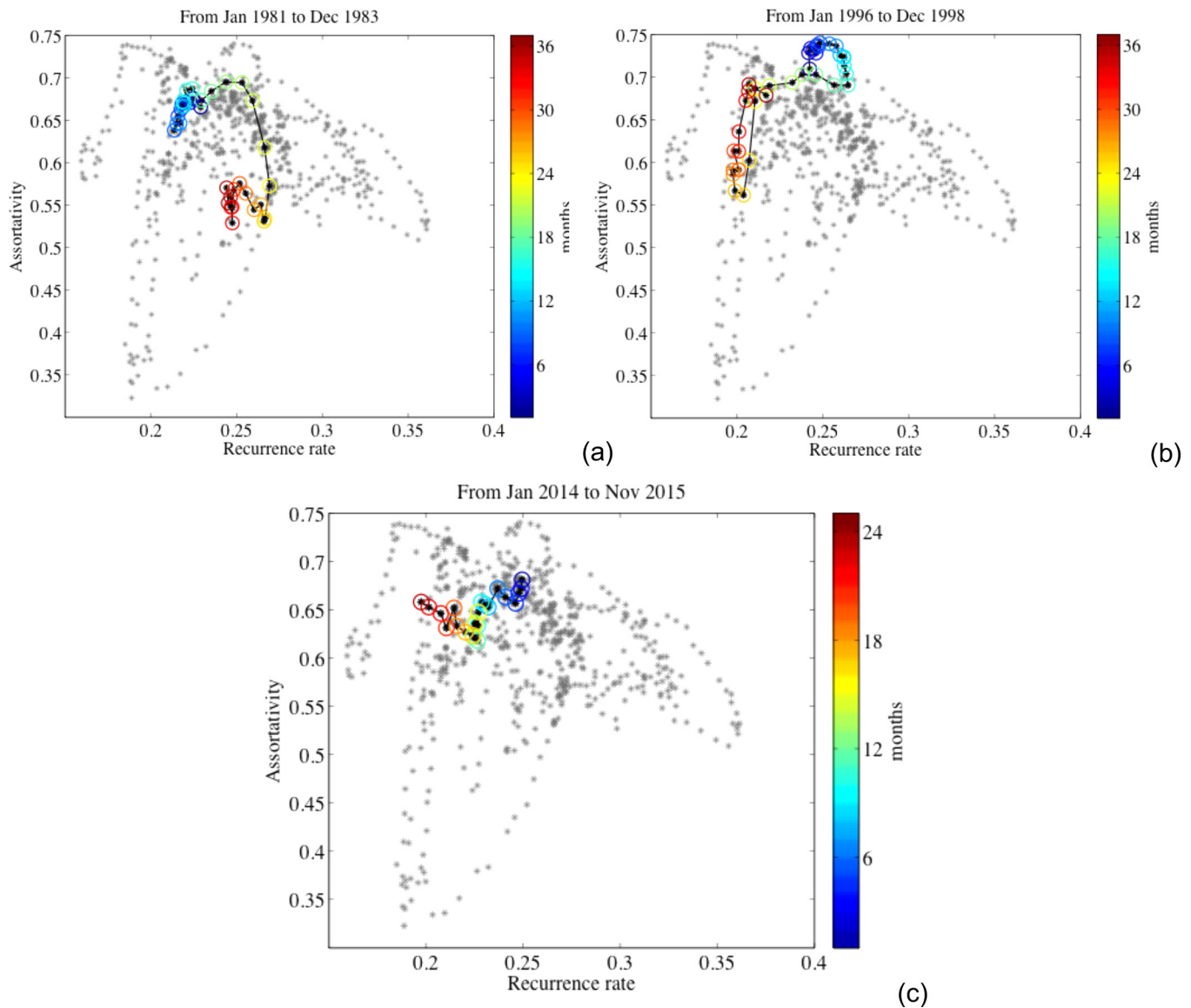
FIG. 9. (a) The scatter plot of the recurrence rate versus assortativity of the RCNs reconstructed from observed SST. A low (high) recurrence rate and high (low) assortativity indicate an unstable (stable) Pacific climate state. The colored circles highlight the development from January 1981 to December 1983. (b) Same as (a) but from January 1996 to December 1998. (c) Same as (a) but from January 2014 to November 2015. The recurrence networks are reconstructed from a 10-year sliding window of the HadISST data.

the background state becomes unstable. This holds also for the BJ index which needs at least 20 years of data and hence will include several events.

The results in Fig. 7 nicely indicate the problems which are faced regarding El Niño predictions. Noise, here through westerly wind bursts, is important to induce SST anomalies, but whether an El Niño will develop depends on the Pacific climate stability that varies on decadal time scales. One can have an El Niño when noise is large even with a stable background (as in 1968), and also an El Niño when background stability is low even without high noise variability (such as in 1992). The lower stability and higher noise variability might be one of the reasons that the 1997 event developed into the "El Niño of the 20th century."

From Fig. 7, it is also interesting to see that the S_d index is relatively high at the beginning of the year 2014, indicating that the Pacific climate state is relatively stable. This is

consistent with the fact that although large subsurface temperature anomalies developed in March 2014, there was no growth of SST anomalies because the thermocline feedback was weak and no strong El Niño event could develop. However, at the beginning of the year 2015, both the S_d index and the recurrence rate decreased, the system was pushed into the supercritical regime and a strong El Niño event developed in 2015.

With this work, we have added to the number of studies[31–33] that indicate that climate network based properties can be very useful analysis tools in ENSO dynamics and prediction. Here, easily calculable measures from PCCNs and RCNs were developed to diagnose the stability of the Pacific background state. We hope that these measures will be used in future studies and will eventually help to improve the skill of predictions of El Niño events over the next decades.

SUPPLEMENTARY MATERIAL

See supplementary material for the BJ index calculation for the ZC-model results.

[1]M. McPhaden, Nat. Clim. Change **5**, 791 (2015).
[2]S. E. Zebiak and M. A. Cane, Mon. Weather Rev. **115**, 2262 (1987).
[3]J. Neelin, D. S. Battisti, A. C. Hirst, F.-F. Jin, Y. Wakata, T. Yamagata, and S. E. Zebiak, J. Geophys. Res. **103**, 14261, doi:10.1029/97JC03424 (1998).
[4]F.-F. Jin, J. Atmos. Sci. **54**, 830 (1997).
[5]A. V. Fedorov and S. G. Philander, Science **288**, 1997 (2000).
[6]L. Bejarano and F.-F. Jin, J. Clim. **21**, 3051 (2008).
[7]F.-F. Jin, J. Neelin, and M. Ghil, Physica D **98**, 442 (1996).
[8]P. C. F. Van der Vaart, H. A. Dijkstra, and F.-F. Jin, J. Atmos. Sci. **57**, 967 (2000).
[9]C. Penland, Physica D **98**, 534 (1996).
[10]G. Burgers, Clim. Dyn. **15**, 521 (1999).
[11]T. Lian, D. Chen, Y. Tang, and Q. Wu, Geophys. Res. Lett. **41**, 3522, doi:10.1002/2014GL059989 (2014).
[12]I. Eisenman, L. Yu, and E. Tziperman, J. Clim. **18**, 5224 (2005).
[13]M. Roulston and J. Neelin, Geophys. Res. Lett. **27**, 3723, doi:10.1029/2000GL011941 (2000).
[14]H. A. Dijkstra, *Nonlinear Climate Dynamics* (Cambridge University Press, 2013).
[15]C. E. Wieners, W. P. de Ruijter, W. Ridderinkhof, A. S. von der Heydt, and H. A. Dijkstra, J. Climate **29**, 4269–4291 (2016).
[16]S. T. Kim, W. Cai, F.-F. Jin, A. Santoso, L. Wu, E. Guilyardi, and S.-I. An, Nat. Clim. Change **4**, 786 (2014).
[17]S. T. Kim and F.-F. Jin, Clim. Dyn. **36**, 1593 (2011).
[18]S. T. Kim and F.-F. Jin, Clim. Dyn. **36**, 1609 (2011).
[19]F.-F. Jin, S. T. Kim, and L. Bejarano, Geophys. Res. Lett. **33**, 23, doi:10.1029/2006GL027221 (2006).
[20]A. Fedorov, S. Harper, S. Philander, B. Winter, and A. Wittenberg, Bull. Am. Meteorol. Soc. **84**, 911 (2003).
[21]D. Chen, M. A. Cane, A. Kaplan, S. E. Zebiak, and D. Huang, Nature **428**, 733 (2004).
[22]S.-W. Yeh, J.-S. Kug, B. Dewitte, M.-H. Kwon, B. P. Kirtman, and F.-F. Jin, Nature **461**, 511 (2009).
[23]A. A. Tsonis and P. J. Roebber, Physica A **333**, 497 (2004).
[24]K. Steinhaeuser, A. R. Ganguly, and N. V. Chawla, Clim. Dyn. **39**, 889 (2012).
[25]A. Tantet and H. A. Dijkstra, Earth Syst. Dyn. **5**, 1–14 (2014).
[26]J. F. Donges, Y. Zou, N. Marwan, and J. Kurths, Eur. Phys. J. - Spec. Top. **174**, 157 (2009).
[27]A. A. Tsonis and K. L. Swanson, Bull. Am. Meteorol. Soc. **87**, 585 (2006).
[28]K. Yamasaki, O. Gazit, and S. Havlin, Europhys. Lett. **83**, 28005 (2008).
[29]J. F. Donges, J. Heitzig, B. Beronov, M. Wiedermann, J. Runge, Q. Y. Feng, L. Tupikina, V. Stolbova, R. V. Donner, N. Marwan, H. A. Dijkstra, and J. Kurths, Chaos **25**, 113101 (2015).
[30]H. Ihshaish, A. Tantet, J. C. M. Dijkzeul, and H. A. Dijkstra, Geosci. Model Dev. **8**, 3321 (2015).
[31]A. Gozolchiani, S. Havlin, and K. Yamasaki, Phys. Rev. Lett. **107**, 148501 (2011).
[32]J. Ludescher, A. Gozolchiani, M. I. Bogachev, A. Bunde, S. Havlin, and H. J. Schellnhuber, Proc. Natl. Acad. Sci. U.S.A. **110**, 11742 (2013).
[33]I. Fountalis, A. Bracco, and C. Dovrolis, Clim. Dyn. **45**, 511 (2015).
[34]A. Von der Heydt, A. Nnafie, and H. Dijkstra, Clim. Past **7**, 903 (2011).
[35]A. E. Gill, Q. J. R. Meteorol. Soc. **106**, 447 (1980).
[36]H. A. Dijkstra and J. Neelin, J. Clim. **8**, 1343 (1995).
[37]N. A. Rayner, D. E. Parker, E. B. Horton, C. K. Folland, L. V. Alexander, D. P. Rowell, E. C. Kent, and A. Kaplan, J. Geophys. Res. **108**, 4407, doi:10.1029/2002JD002670 (2003).
[38]K. E. Taylor, R. J. Stouffer, and G. A. Meehl, Bull. Am. Meteorol. Soc. **93**, 485 (2012).
[39]R. W. Katz, Stat. Sci. **17**, 97 (2002).
[40]K. Steinhaeuser, N. V. Chawla, and A. R. Ganguly, ACM SIGKDD Explor. Newsl. **12**, 25 (2010).
[41]J. F. Donges, "Functional network macroscopes for probing past and present Earth system dynamics," Ph.D. thesis (Humboldt-Universität zu Berlin, Mathematisch-Naturwissenschaftliche Fakultät I, 2013).
[42]Q. Y. Feng and H. Dijkstra, Geophys. Res. Lett. **41**, 541, doi:10.1002/2013GL058687 (2014).
[43]J.-P. Eckmann, S. O. Kamphorst, and D. Ruelle, Europhys. Lett. **4**, 973 (1987).
[44]N. Marwan, M. C. Romano, M. Thiel, and J. Kurths, Phys. Rep. **438**, 237 (2007).
[45]N. Marwan, J. F. Donges, Y. Zou, R. V. Donner, and J. Kurths, Phys. Lett. A **373**, 4246 (2009).
[46]J. Donges, R. Donner, K. Rehfeld, N. Marwan, M. Trauth, and J. Kurths, Nonlinear Processes Geophys. **18**, 545 (2011).
[47]R. V. Donner, Y. Zou, J. F. Donges, N. Marwan *et al.*, New J. Phys. **12**, 033025 (2010).
[48]Y. Zou, R. V. Donner, M. Wickramasinghe, I. Z. Kiss, M. Small, and J. Kurths, Chaos **22**, 033130 (2012).
[49]M. E. Newman, Phys. Rev. Lett. **89**, 208701 (2002).
[50]T. M. Smith and R. W. Reynolds, J. Clim. **16**, 1495 (2003).
[51]D. Legler and J. O'Brien, Intergovernmental Oceanographic Commission 11 (1988).
[52]C. E. Menkes, M. Lengaigne, J. Vialard, M. Puy, P. Marchesiello, S. Cravatte, and G. Cambon, Geophys. Res. Lett. **41**, 6476, doi:10.1002/2014GL061186 (2014).
[53]M. Mheen, H. A. Dijkstra, A. Gozolchiani, M. den Toom, J. Feng, Q. Kurths, and E. Hernandez-Garcia, Geophys. Res. Lett. **40**, 2714, doi:10.1002/grl.50515 (2013).
[54]Q. Y. Feng, J. P. Viebahn, and H. A. Dijkstra, Geophys. Res. Lett. **41**, 6009, doi:10.1002/2014GL061019 (2014).
[55]R. A. Fisher, Biometrika **10**, 507 (1915).
[56]A. J. Faller, J. Appl. Meteorol. **20**, 203 (1981).
[57]E. Kalnay, M. Kanamitsu, R. Kistler, W. Collins, D. Deaven, L. Gandin, M. Iredell, S. Saha, G. White, J. Woollen *et al.*, Bull. Am. Meteorol. Soc. **77**, 437 (1996).
[58]F.-F. Jin and J. Neelin, J. Atmos. Sci. **50**, 3477 (1993).
[59]J. F. Donges, Y. Zou, N. Marwan, and J. Kurths, Europhys. Lett. **87**, 48007 (2009).